Simulation of operation of an NH₃-laser-based multiwave remote gas analyzer

V.A. Banakh, Yu.N. Ponomarev, I.N. Smalikho, K.M. Firsov, D.D. Malyuta, and G.A. Polyakov

Institute of Atmospheric Optics,
Siberian Branch of the Russian Academy of Sciences, Tomsk
Troitsk Institute of Innovation and Thermonuclear Investigations

Operation of an NH₃-laser-based multiwave remote gas-analyzer is simulated by the Monte Carlo method. The potentialities of such a gas analyzer are investigated for ground paths with a retroreflector, and main sources of errors are analyzed for operation through the turbulent atmosphere.

Introduction

Remote laser gas analyzers and differential absorption lidars for monitoring of the atmospheric composition are now actively developed in many countries.[1,2]

Analytical laser systems based on repetitively pulsed mid-infrared tunable lasers are promising for remote detection and estimation of a content of various molecular compounds polluting the atmosphere at the level of ppm and ppb.

Among different spectroscopic phenomena, such as resonance absorption, Raman scattering, laser-induced fluorescence, the resonance absorption is characterized by the largest cross section of interaction with radiation in the IR region. Therefore, laser methods utilizing this effect have high sensitivity.

The use of multiwave molecular gas lasers (CO_2, HF, DF, CO, NH₃, and others) in remote gas analyzers provides the possibility to remotely determine concentrations of different atmospheric pollutants at the same time, even under conditions of incomplete beam interception at an open path with a retroreflector.

The NH₃ optically pumped laser provides for simultaneous lasing at a large number of wavelengths (10 to 30) as a collinear beam, hereby over the 11 – 14 μm range it provides the possibility to monitor several molecular constituents of air, including vapors of toxic agents and emissions of nuclear industries.[3]

Current concepts on the processes of laser radiation interaction with the atmosphere, available spectroscopic information, and numerical methods developed allow one to simulate the operation of a multiwave remote gas analyzer (or lidar) in the actual turbulent atmosphere containing an aerosol component and gaseous pollutants to be monitored. Numerical experiments permit not only detailed study of all the factors affecting power characteristics of the sounding laser beam, but also optimization of the

analyzer design and the technique for solution of the inverse problem, i.e., the technique for reconstruction of the number density of the gases to be determined.

In this work, the operation of an NH₃-laser-based remote gas analyzer along paths up to 4 km long with a retroreflector (mirror or topographic target) has been simulated by the Monte Carlo method allowing for absorption and scattering by molecules and aerosol, as well as turbulent distortions of a beam. The potentialities of this analyzer have been evaluated, and the main sources of errors have been analyzed.

Operating principle and design of the multiwave remote gas analyzer

The principal difference of the remote gas-analyzer with an NH₃ laser from the most popular systems utilizing CO_2 lasers is that the NH₃ laser operates simultaneously at a large number of transitions (up to 30), so radiation intensities at the beginning and at the end of the measuring path should be compared simultaneously for each wavelength. The emitted radiation intensity spectrum is controlled by a diffraction-type polychromator. Upon passage of the radiation through the sounded volume and reflection from the retroreflector of a topographic object (or scattering at atmospheric aerosol particles), it is collected by the receiving telescope and analyzed by the same polychromator. After analysis of the transmission spectrum at each wavelength, the atmospheric composition and pollutant concentration along the path are determined.

Figure 1 shows the optical arrangement of the remote gas analyzer operating at the path with a retroreflector. The basic characteristics of the NH₃ laser are the following:

  – output power: 1 kW;
  – pulse duration: 300 ns – 1μs;
  – width of a separate line: less than 150 MHz;
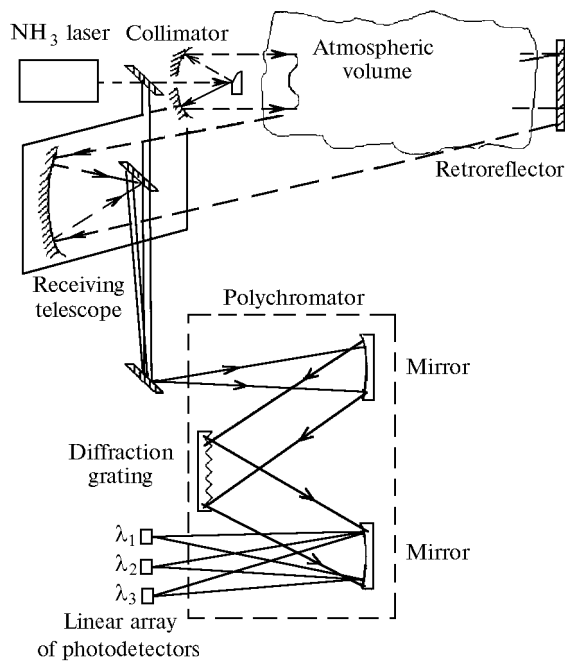 – angular divergence of a beam: $5 \cdot 10^{-3} - 5 \cdot 10^{-4}$ rad.

Fig. 1. Receiving system of the NH_3 lidar.

Laser radiation at the output from the sounded atmospheric volume was collected by the Cassegrainian telescope and focused at the entrance slit of the diffraction polychromator. The linear array of photodetectors was set in the plane of the exit slit; it served to record the entire radiation spectrum and changes in the intensity at each line as a result of radiation extinction in the atmosphere.

The laser spectrum was controlled by varying the pressure and composition of the lasant.[3] The intensity of an individual laser line depends on the NH_3/N_2 concentration ratio. As the N_2 content in the lasant increases, the laser intensity decreases in the longwave part of the spectrum and increases in the shortwave part.

The numerical simulation was performed for the following conditions:

Composition of the multicomponent gas medium: NH_3, HCN, HNO_3, CO_2, and H_2O with the CO_2 and H_2O concentrations typical of the standard atmosphere at the ground paths.

Parameters of the sounding path: horizontal, 2 km long from the transceiving telescope to the retroreflector (that is, the complete path length was 4 km); distribution of gaseous constituents was taken homogeneous; or the case of an area 50 − 100 m in size with sharply increased concentration of one component gas was considered. Fluctuations in concentrations of absorbing substances along the path were considered as determined by random temperature and pressure fluctuations, including the case of allowing for the effect of turbulence along the path.

Receiving optics includes the Cassegrainian telescope (30 cm in diameter and 2 m in focal length) and the diffraction polychromator. The geometry of the receiving system is shown in Fig. 2.
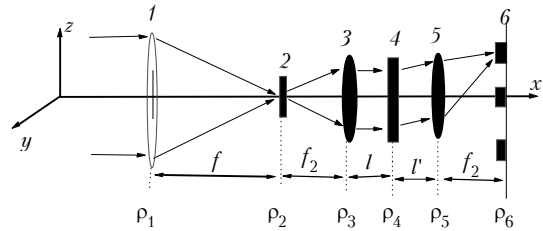

Fig. 2. Optical arrangement of the receiving system.

In the considered telescope an objective serves as an aperture diaphragm of the annular type. In this case the properties of the objective as a diffraction limited system are determined by the pupil function $P_t(z, y)$ which can be presented as below following from the design of the Cassegrainian objective:

$$P_t(z, y) = \begin{cases} 1, & r_0 \le r \le a_t, \\ 0, & r_0 > r > a_t, \end{cases} \quad (1)$$

where $r = (z^2 + y^2)^{1/2}$; $a_t = 15$ cm is the outer radius; r_0 is the inner radius determined by the mirror size at the input of the telescope. In the following calculations the inner radius is $r_0 = 5$ cm. The entrance slit of the polychromator is set vertically in the focal plane of the telescope. The transfer function of the slit is determined as

$$P_s(z, y) = P_s(y) = \begin{cases} 1, & |y| \le r_s/2, \\ 0, & |y| > r_s/2, \end{cases} \quad (2)$$

where r_s is the slit width.

The collimating lens with the focal length $f_2 = 50$ cm is placed beyond the slit at the distance f_2. The 100×100 mm diffraction grating (100 lines/mm) is set at an angle θ_0 with the optical axis. The angle between the optical axis of the lens collecting the radiation reflected by the grating and the normal to the grating plane is denoted as θ_1. In accordance with Ref. 4, the angle θ corresponding to the maximum first-order intensity of the plane wave radiation scattered by the grating at the wavelength λ_0 is determined as

$$\sin\theta_0 + \sin\theta = \lambda_0/d, \quad (3)$$

where d is the grating period.

For $\theta_0 = \theta$ we obtain

$$\theta_0 = \arcsin(\lambda_0/2d). \quad (4)$$

So $\theta_0 = 44.43°$ for $d = 10$ μm and $\lambda_0 = 14$ μm, and $\theta_0 = 33.37°$ for $\lambda_0 = 11$ μm.

In the chosen scheme the transfer function of the diffraction grating for the incident radiation with an arbitrary wavelength λ can be written as

$$P_d(z, y) = P_d(y) = \exp\left\{-2\pi j \frac{2\sin\theta_0}{\lambda} y\right\} \times$$

$$\times \sum_{l=-n}^{n} Q(y + ld), \quad (5)$$

where $Q(y) = \begin{cases} 1, & |y| \le d/4, \\ 0, & |y| > d/4; \end{cases}$ $N = 2n + 1$ is the number of grooves.

In accordance with the designations in Fig. 2 the distance between the plane of collimating lens *3* and the diffraction grating is l, that between the diffraction grating and the plane of lens *5* is l', and the focal length of this lens set beyond the diffraction grating is $f_2 = 50$ cm. The linear array of photodetectors is placed in the focal plane of lens *5*.

Algorithm for calculation of intensity distribution in the planes of optical elements of the receiving system

Let $\rho_i = \{z_i, y_i\}$ denote the coordinates in the plane of optical elements of the system shown in Fig. 2, $i = 1, 2, ..., 6$. The complex amplitude of the field of light wave with the wavelength λ in the ith plane is designated as $E_i(\rho_i)$.

The parameter $E_1(\rho_1)$ describes the distribution of the complex amplitude of the field of the wave having passed through the atmospheric channel in the plane of the telescope objective; $E_2(\rho_2)$ is the field amplitude at the entrance slit of the polychromator:

$$E_2(\rho_2) = \frac{k}{2\pi j f} \int d^2\rho_1 \, E_1(\rho_1) \, P_t(\rho_1) \times$$

$$\times \exp\left\{-j \frac{k}{2f} \rho_1^2 + j \frac{k}{2f} (\rho_1 - \rho_2)^2\right\}. \quad (6)$$

In the plane of lens *3* the complex amplitude of the field is described by the equation

$$E_3(\rho_3) = \frac{k}{2\pi j f_2} \int d^2\rho_2 \, E_2(\rho_2) \, P_s(\rho_2) \times$$

$$\times \exp\left\{j \frac{k}{2f_2} (\rho_2 - \rho_3)^2\right\}. \quad (7)$$

The diameter of lens *3* is assumed to be longer than the transverse dimension of the light beam. In this case $E_4(\rho_4)$ and $E_3(\rho_3)$ are related to each other as

$$E_4(\rho_4) = \frac{k}{2\pi l j} \int d^2\rho_3 \, E_3(\rho_3) \times$$

$$\times \exp\left\{-j \frac{k}{2f_2} \rho_3^2 + j \frac{k}{2l} (\rho_3 - \rho_4)^2\right\}. \quad (8)$$

Upon passage of the light wave through the diffraction grating, the distribution of the field amplitude in the plane of lens *5* is described by the equation

$$E_5(\rho_5) = \frac{k}{2\pi j l'} \int d^2\rho_4 \, E_4(\rho_4) \, P_d(\rho_4) \times$$

$$\times \exp\left\{j \frac{k}{2\pi l'} (\rho_4 - \rho_5)^2\right\}. \quad (9)$$

And, finally, in the plane of the exit slit (linear array of photodetectors) it has the form

$$E_6(\rho_6) = \frac{k}{2\pi j f_2} \int d^2\rho_5 \, E_5(\rho_5) \times$$

$$\times \exp\left\{-j \frac{k}{2f_2} \rho_5^2 + j \frac{k}{2f_2} (\rho_5 - \rho_6)^2\right\}. \quad (10)$$

The instantaneous distribution of beam intensities in the plane of the entrance slit (ρ_2), diffraction grating (ρ_4), and photodetector array (ρ_6) was simulated by the following scheme. Assuming $l = f_2 + f_2^2/f$ and using Eqs. (6)–(10), for the intensities $I_i(\rho_i) = |E_i(\rho_i)|^2$ we have the following equations:

$$I_2(\rho_2) = |A(\rho_2)|^2, \quad (11)$$

where

$$A(\rho_2) = \frac{1}{j\lambda f} \int d^2\rho_1 E_1(\rho_1) P_t(\rho_1) \exp\left\{-2\pi j \frac{\rho_2\rho_1}{\lambda f}\right\}; \quad (12)$$

$$I_4(\rho_4) = |E_4(\rho_4)|^2, \quad (13)$$

$$E_4(\rho_4) = \frac{1}{j\lambda f_2} \int d^2\rho_2 \, A(\rho_2) P_s(\rho_2) \exp\left\{-2\pi j \frac{\rho_4\rho_2}{\lambda f_2}\right\}; \quad (14)$$

and

$$I_6(\rho_6) = |B(\rho_6)|^2, \quad (15)$$

where

$$B(\rho_6) = \frac{1}{j\lambda f_2} \int d^2\rho_4 E_4(\rho_4) P_d(\rho_4) \exp\left\{-2\pi j \frac{\rho_6\rho_4}{\lambda f_2}\right\}. \quad (16)$$

The analysis of Eqs. (1)–(16) shows that in the absence of the entrance slit ($P_s(\rho_2) \equiv 1$) the intensity in the plane of the detector array is

$$I_6(\rho_6) = I_2(-\rho_6) P_s(-\rho_6). \quad (17)$$

Because of diffraction at the grating, the maxima in the intensities of the laser beam at different wavelengths become spatially resolved.

Using Eqs. (2), (5), and (14), Eq. (16) can be simplified as:

$$B(z_6, y_6) = \frac{1}{j\lambda f_2} \int_{-r_s/2}^{r_s/2} dy_2 \, A(-z_6, y_2) \times$$

$$\times \frac{d}{2} \text{sinc}\left(\frac{\pi}{2} \xi\right) \frac{\sin(N\pi\xi)}{\sin(\pi\xi)}, \quad (18)$$

where $\text{sinc}(x) = \sin x / x$;

$$\xi = \frac{d}{\lambda}\left(\frac{y_6 + y_2}{f_2}\right) + 2\sin\theta_0.$$

In the limiting case of a very narrow slit $r_s \to 0$ we can assume $A(-z_6, y_2) \approx A(-z_6, 0)$ and $\xi \approx (y_6/f_2 + 2\sin\theta_0)d/\lambda$ in Eq. (18) and obtain

$$I_6(z_6, y_6) = \frac{I_2(-z_6, 0)}{(\lambda f_2)^2}\left(\frac{r_s d}{2}\right)^2 \times$$

$$\times \text{sinc}^2\left(\frac{\pi}{2}\eta\right) \frac{\sin^2(N\pi\eta)}{\sin^2(\pi\eta)}, \quad (19)$$

where $\eta = (y_6/f_2 + 2\sin\theta_0)d/\lambda$.

The position of the diffraction maxima is determined from the equation $\eta = 1$, therefrom it follows that

$$y_6 = f_2 \left[\lambda / d - 2\sin\theta_0 \right]. \qquad (20)$$

Taking into consideration Eq. (4), the last equation can be presented as

$$y_6 = f_2 (\lambda - \lambda_0) / d. \qquad (21)$$

Therefore, for $\lambda = \lambda_0$ the intensity maximum coincides with the optical axis ($y_6 = 0$).

Let us estimate the distance d_p between two intensity maxima corresponding to two wavelengths differing by $\Delta\nu = 0.3$ cm^{-1} assuming $\lambda = 14$ μm and $\lambda_0 < \lambda$. After substitution of $\lambda - \lambda_0 = \lambda \left[1 - (1 + \lambda\Delta\nu / 10^4)^{-1} \right]$ in Eq. (21) we obtain $d_p = 0.3$ mm. The size of a spot for the laser beam with the wavelength λ equals $f_2\lambda / L_d$ (where $L_d = N{\cdot}d = 10$ cm is the size of the diffraction grating). For $\lambda = 14$ μm this size equals 0.07 mm. Hence, detectors with the receiving area of 0.15×0.15 mm are suitable for reliable resolution of intensity peaks by the polychromator with the characteristics considered.

It is easy to estimate the size of the spot in the plane of the entrance slit in the absence of atmospheric turbulence. It equals 0.075 mm. It follows herefrom that to decrease energy losses, the width of the entrance slit must be no less than 0.15 mm. Such size of the entrance slit and a single photodetector in the linear array guarantee good resolution and minimal energy losses under conditions of very weak turbulence. It is clear that for stronger turbulence the spot size at the entrance slit grows, and the increase in energy losses for the slit 0.15 mm wide is inevitable.

Propagation of the NH$_3$-laser beam in the turbulent atmosphere was modeled using the methods of numerical simulation. Equations (11)−(16) describing the instantaneous intensity distribution of laser radiation in the telescope focal plane (at the entrance slit) and at the diffraction grating allow the fast Fourier transform method to be applied for numerical simulation. To calculate the field in the objective plane of the telescope at the entrance slit and in the grating plane, the different grid step Δh was used. The calculated signal $S(\lambda)$ was normalized against its corresponding value in the absence of turbulence

$$S(\lambda) = \frac{\displaystyle\int\limits_{-D/2}^{D/2}\!\!\int dz_6 \, dy_6 \, I_6(z_6, y_6 - y_m(\lambda))}{\displaystyle\int\limits_{-D/2}^{D/2}\!\!\int dz_6 \, dy_6 \, I_6^0(z_6, y_6 - y_m(\lambda))}, \qquad (22)$$

where $y_m(\lambda) = f_2(\lambda - \lambda_0) / d$ and $I_6^0(z_6, y_6)$ is the radiation intensity distribution at the linear array of photodetectors in the absence of turbulence.

The series of numerical experiments gave the data on instantaneous intensity distributions in the objective plane and focal plane of the telescope at the diffraction grating and linear array of photodetectors. In calculations the width of the entrance slit was varied from 0.1 to 1 mm. The laser wavelengths $\lambda_1 = 14$, $\lambda_2 = 13.99412$, $\lambda_3 = 13.98825$, and $\lambda_4 = 13.98238$ μm met the condition $\lambda_{I+1} - \lambda_i \approx 0.006$ μm ($\Delta\nu = 0.3$ cm^{-1}).

Simulation of laser beam propagation through the turbulent atmosphere

To calculate a random distribution of the complex amplitude of the laser beam along the path in the turbulent atmosphere, the algorithm of random phase screens was used. The detailed description of this algorithm can be found, for example, in Ref. 5. The idea of the method is that the atmospheric path with the length x is divided into N_x layers each Δx thick. A random phase screen is set at the entrance of each layer. Passing through this screen, the beam experiences phase distortion, i.e., its complex amplitude $E(x_i, \rho)$ is multiplied by $\exp\{j\psi(x_i, \rho)\}$, where ψ is the random phase; $x_i = i\Delta x$, $i = 0,\ldots,N_x - 1$, and $\rho = \{x, y\}$ is the coordinate in the plane perpendicular to the beam propagation direction.

Then the beam diffraction within each layer is calculated by the fast Fourier transform method

$$E(x_{i+1}, \rho) = F^{-1}\left\{ \exp\left[-j\, \frac{(2\pi)^2 \Delta x}{2k} \, \kappa^2 \right] \times \right.$$
$$\left. \times F\left[E(x_i, \rho)\, e^{j\psi} \right] \right\}, \qquad (23)$$

where F and F^{-1} correspond to the direct and inverse Fourier transform; $k = 2\pi / \lambda$ is the wave number.

In this case the Karman model[6–8] was used for the power spectrum of phase fluctuations of the wave having passed through the turbulent layer Δx thick:

$$\Phi_\psi(\kappa) = \sigma_\psi^2 \, 0.265226 \, \frac{(8.42 L_n)^2}{[1 + (8.42 L_n)^2 \, \kappa^2]^{11/6}}, \qquad (24)$$

where

$$\sigma_\psi^2 = 1.273 \, C_n^2 \, L_n^{5/3} \, k^2 \Delta x \qquad (25)$$

is the variance of wave phase fluctuations; C_n^2 is the structure constant of the refractive index; L_n is the outer scale of turbulence.

Setting the initial distribution of the field in the laser beam $E(0, \rho)$ and the parameters of the medium C_n^2 and L_n, one can numerically simulate a random distribution of the laser beam intensity along the ground path $x = N_x\Delta x$ long. Averaging by an ensemble of random realizations allows one to calculate different statistical characteristics of the laser beam. This approach can be easily generalized to

the case of multiwave laser beam propagation in a turbulent medium. For this case the centers of photodetector areas should be separated by 0.3 mm.

Figures 3 and 4 show the random intensity distribution for the atmospheric channel without turbulence with $C_n^2 = 0$ (Fig. 3) and for the case of strong turbulence with $C_n^2 = 10^{-12}$ $m^{-2/3}$ (Fig. 4).

Figures 3a and 4a correspond to the polychromator slit width $r_s = 0.45$ mm; Figs. 3b and 4b correspond to $r_s = 0.15$ mm.
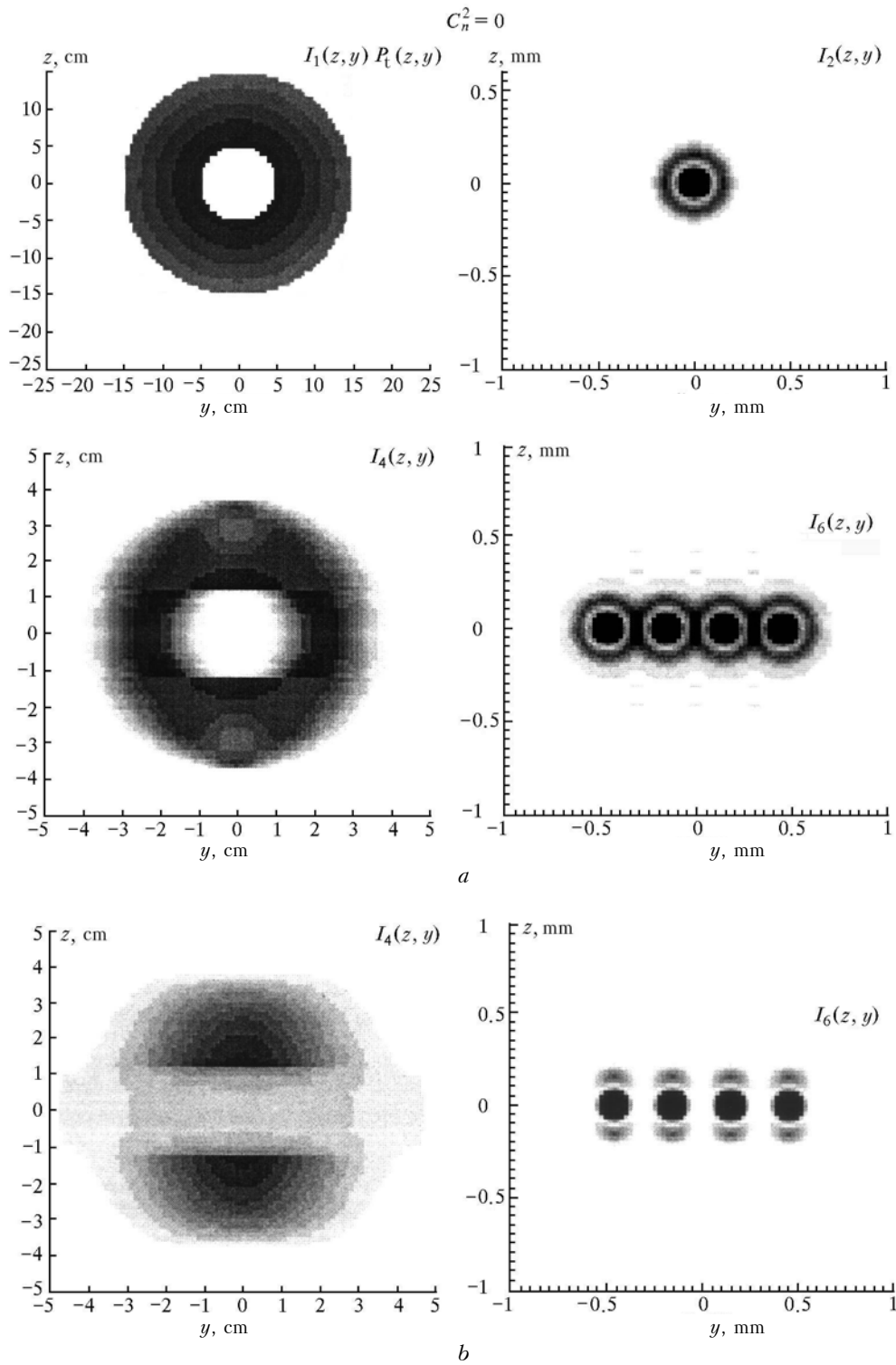
Fig. 3. Beam intensity distribution in the receiving I_1 and focal I_2 planes of the telescope, at the diffraction grating I_4, and in the detector plane I_6 for the slit 0.45 mm (a) and 0.15 mm (b) wide in the absence of turbulence ($C_n^2 = 0$).

$$C_n^2 = 10^{-12} \text{ m}^{-2/3}$$

$I_1(z, y) \, P_t(z, y)$

$I_2(z, y)$

$I_4(z, y)$

$I_6(z, y)$

a

$I_4(z, y)$

$I_6(z, y)$

b

Fig. 4. Instantaneous beam intensity distributions corresponding to the distributions in Fig. 3, but for $C_n^2 = 10^{-12}$ m$^{-2/3}$ (strong turbulence).

Figure 5 shows the pattern of the intensity distribution at the linear array of detectors for different values of C_n^2 and the width of the entrance slit equal to 0.45 and 0.15 mm.
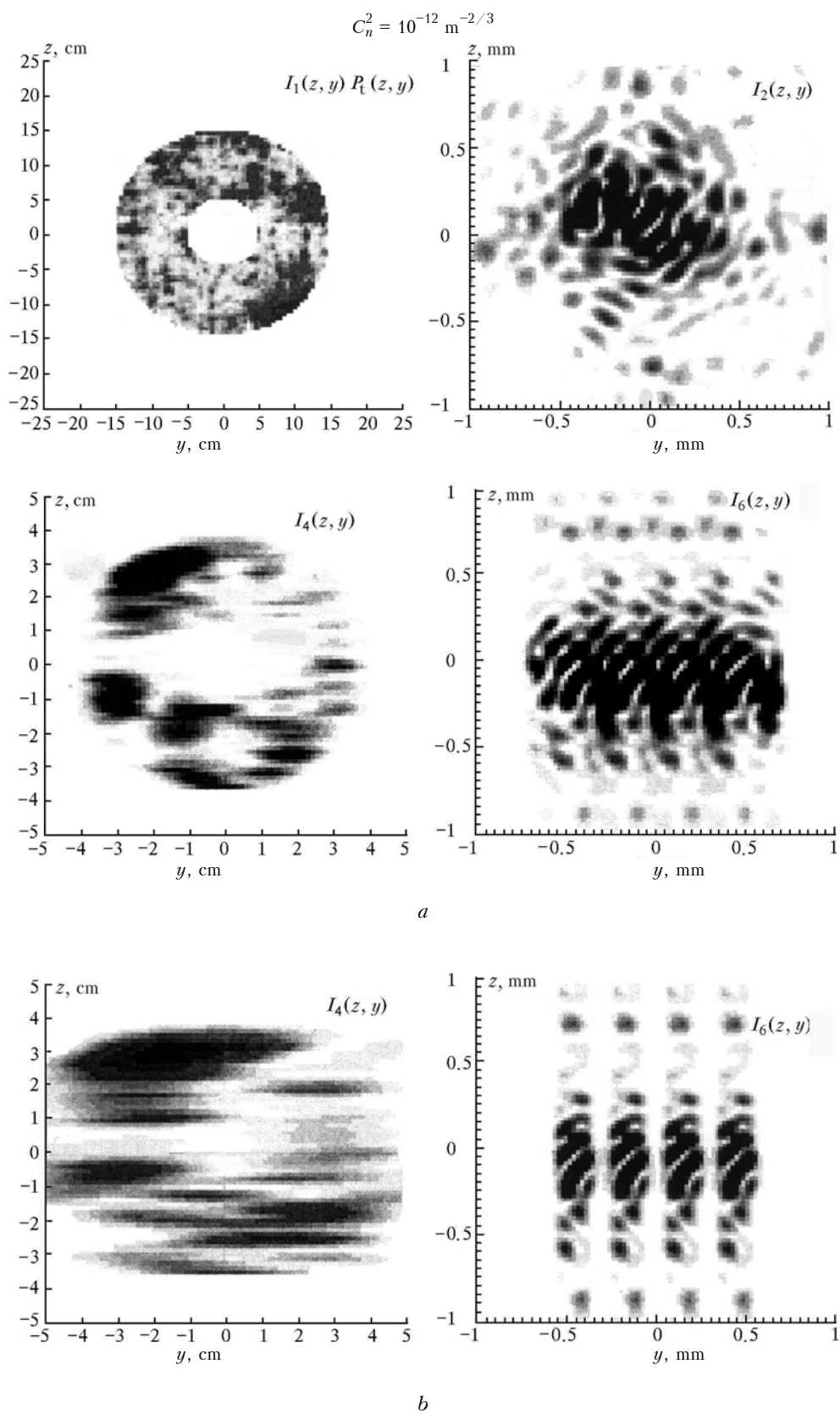
The area occupied by the receiving area $(150 \times 150 \ \mu m)$ of a photodetector is also shown. It is clearly seen from these figures that the slit with the width of 0.45 mm does not provide for resolution of beams with the frequencies separated by 0.3 cm^{-1}, whereas the narrow slit 0.15 mm wide ensures reception of radiation at one of the wavelengths by an element of the linear array of photodetectors.
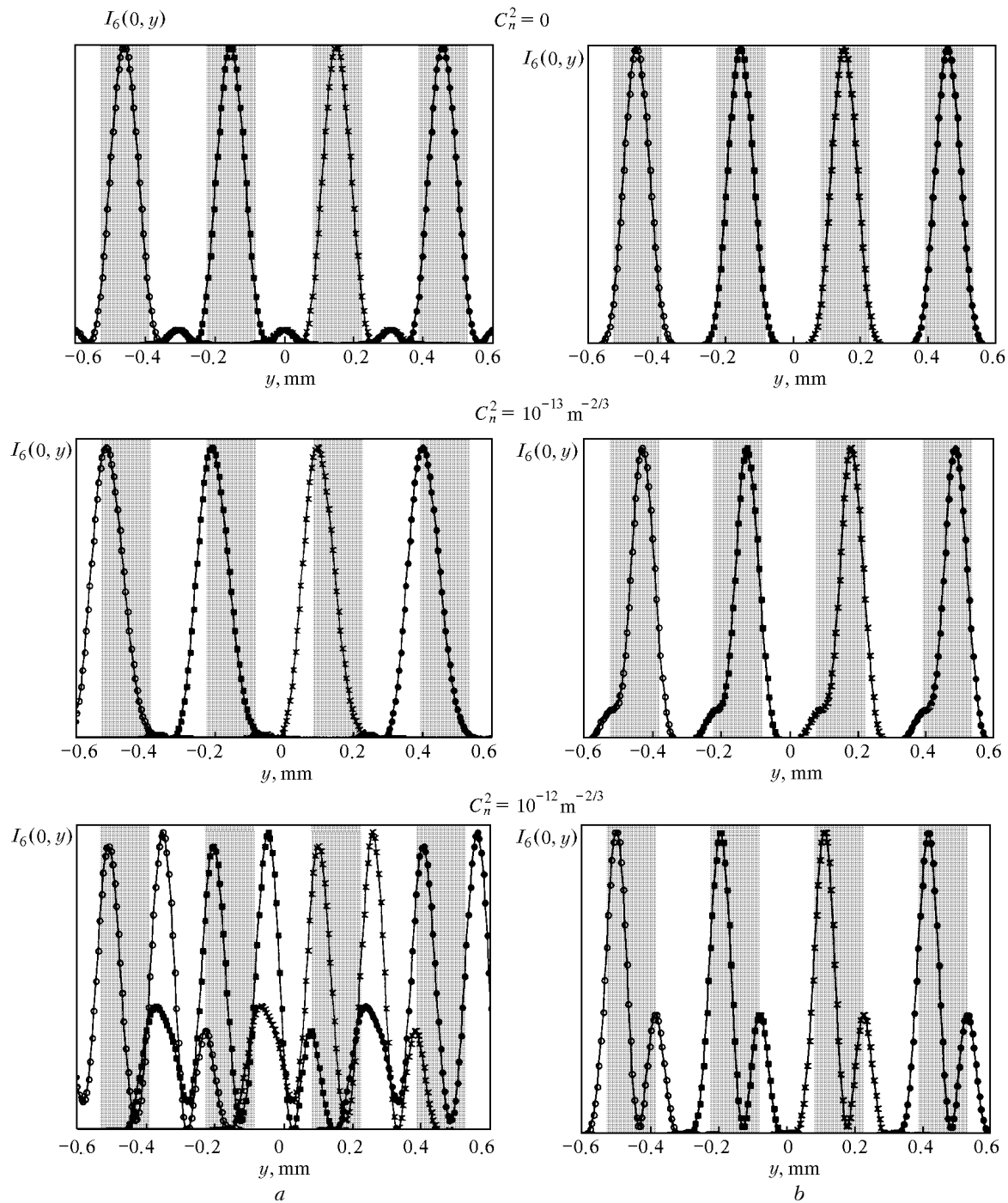

Fig. 5. Instantaneous intensity distributions $I_6(0, y)$ in the plane of detectors for $C_n^2 = 0$, $C_n^2 = 10^{-13}$ m$^{-2/3}$, and $C_n^2 = 10^{-12}$ m$^{-2/3}$; the slit width is 0.45 (a) and 0.15 mm (b).

If the difference between frequencies in the beam increases up to $\Delta\nu = 30$ cm^{-1} (for example, for the set of wavelengths $\lambda_1 = 14$, $\lambda_2 = 13.4357$, $\lambda_3 = 12.9151$, and $\lambda_4 = 12.4334$ μm), the intensity maxima corresponding to these wavelengths are separated in the plane of the photodetector array by 30 mm with the entrance slit 0.15 mm wide. For this case the shape of the intensity distribution for the frequencies separated by 30 cm^{-1} differs markedly (Fig. 6), whereas the shape for the frequencies separated by 0.3 cm^{-1} is identical at the same turbulence (see Fig. 5). An example of calculation of the signal at the photodetector for four wavelengths separated by 30 cm^{-1} is shown in Fig. 7. It is clear from this figure that turbulent distortions of the laser beam can lead to noticeable spectral trends.
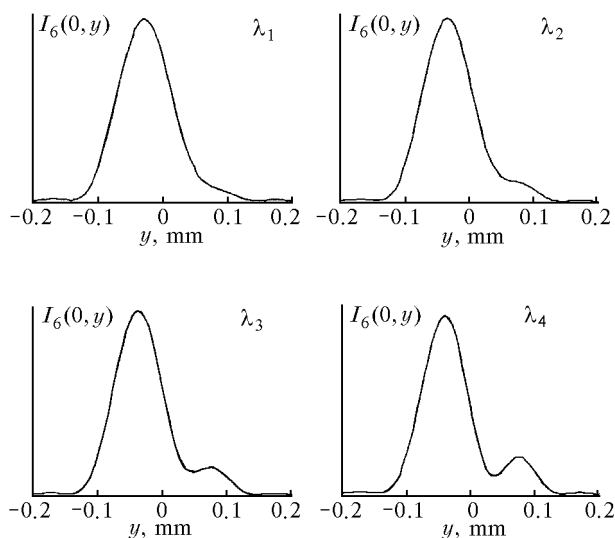

Fig. 6. Instantaneous intensity distributions $I_6(0, y)$ in the detector plane for $C_n^2 = 10^{-12}$ m$^{-2/3}$ and the frequency difference of 30 cm^{-1} ($\lambda_1 = 14$ μm).
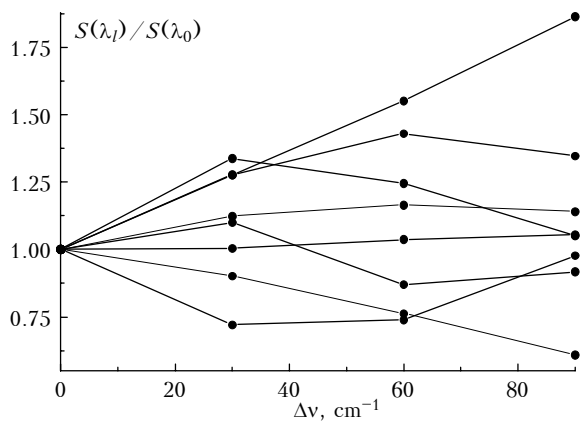

Fig. 7. Spectral dependence of the signal at the photodetector for the case of strong turbulence ($C_n^2 = 10^{-12}$ m$^{-2/3}$) along the path 4 km long.

Statistical analysis of the effect of turbulence on laser beam distortion at the horizontal path

For our consideration of the results of statistical analysis of the turbulence effect on a laser beam propagating along an atmospheric path to be more descriptive and convenient, let us introduce (by analogy with the optical depth) the following parameter: logarithmic loss factor (LLF) $\tau_i^p = -\ln(T_i^p)$ for the ith wavelength. Table 1 presents the data on the mean values of LLF for the used set of wavelengths at different sample size. The samples for different wavelengths with the same C_n^2 parameter were checked for homogeneity against the Kolmogorov−Smirnov criterion. The results of the check showed that the samples for different wavelengths are indistinguishable. The only exclusion was two samples of size $N = 800$ with $\lambda_1 = 14$ and $\lambda_4 = 12.4334$ μm ($C_n^2 = 10^{-13}$ m$^{-2/3}$) which differ only slightly. This allows us to conclude that in the case of moderate turbulence the first and second moments of the intensity fluctuation distribution have weak spectral dependence, and in the case of strong turbulence at the frequency interval up to 90 cm^{-1} the spectral dependence of LLF can be neglected.

Table 1. Descriptive statistics of τ_i^p (N is the sample size)

Wave-length, μm	Mean	Min	Max	rms*	Standard deviation
$C_n^2 = 10^{-12}$ m$^{-2/3}$ ($N = 800$)					
14	6.16	3.33	10.10	1.17	0.04
13.4357	6.18	3.35	10.75	1.17	0.04
12.9151	6.20	3.37	10.54	1.15	0.04
12.4334	6.21	3.42	10.81	1.15	0.04
$C_n^2 = 10^{-13}$ m$^{-2/3}$ ($N = 800$)					
14	3.67	2.78	5.58	0.47	0.02
13.4357	3.68	2.77	5.70	0.48	0.02
12.9151	3.71	2.78	5.82	0.50	0.02
12.4334	3.73	2.78	5.94	0.52	0.02
$C_n^2 = 10^{-14}$ m$^{-2/3}$ ($N = 200$)					
14	3.45	3.08	3.92	0.14	0.01
13.4357	3.45	3.08	3.92	0.14	0.01
12.9151	3.45	3.08	3.91	0.14	0.01
12.4334	3.45	3.08	3.90	0.14	0.01

* root-mean-square deviation.

To determine the type of the LLF distribution, the histograms were constructed. Besides, it was checked by the χ^2 criterion which of three distributions (normal, lognormal, or gamma distribution) the LLF statistics satisfies to. It turned out that in the case of strong ($C_n^2 = 10^{-12}$ m$^{-2/3}$) and weak ($C_n^2 = 10^{-14}$ m$^{-2/3}$) turbulence the LLF statistics is described by the normal distribution for all λ_i.

In the intermediate case of moderate turbulence ($C_n^2 = 10^{-13}$ m$^{-2/3}$) all the above-mentioned types of distribution failed to describe the LLF statistics

(Fig. 8). The calculated LLF distribution density proved to be more asymmetric than in the case of the lognormal and gamma distribution for all the wavelengths tested.

The calculated results on the correlation coefficients between the loss coefficients at different wavelengths $R^p(\lambda_m, \lambda_n)$ are given in Table 2, while Table 3 gives $R^p(t_m, t_n)$ in different time at the 14 μm wavelength for the series of sequential laser pulses emitted with the repetition frequency of 10 Hz and for the wind speed equal to 0.5 m/s. These results are valid for any sequence of pulses provided that the condition $l = 0, 5, 10,$ and 15 cm is satisfied, respectively. Here $l = v/f$ (v is the wind speed; f is the pulse repetition frequency).
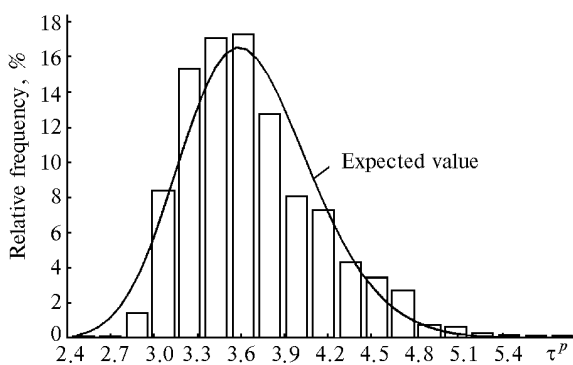

Fig. 8. Distribution density of $\tau_i^p = -\ln(T_i^p)$ ($\lambda_1 = 14$ μm, $C_n^2 = 10^{-13}$ m$^{-2/3}$). The asymmetry coefficient is 0.94 ± 0.09; the excess coefficient is 0.76 ± 0.17.

Table 2. $R^p(\lambda_m, \lambda_n)$

C_n^2, m$^{-2/3}$		λ_1	λ_2	λ_3	λ_4
10^{-14}	λ_1	1.000	1.000	0.999	0.997
	λ_2	1.000	1.000	1.000	0.999
	λ_3	0.999	1.000	1.000	1.000
	λ_4	0.997	0.999	1.000	1.000
10^{-13}	λ_1	1.000	0.999	0.996	0.992
	λ_2	0.999	1.000	0.999	0.997
	λ_3	0.996	0.999	1.000	0.999
	λ_4	0.992	0.997	0.999	1.000
10^{-12}	λ_1	1.000	0.994	0.980	0.963
	λ_2	0.994	1.000	0.993	0.980
	λ_3	0.980	0.993	1.000	0.994
	λ_4	0.963	0.980	0.994	1.000

Table 3. $R^p(t_m, t_n)$ for $\lambda = 14$ μm

C_n^2, m$^{-2/3}$		$t_1(0)$	$t_2(5)$	$t_3(10)$	$t_4(15)$
10^{-13}	t_1	1.000	0.751	0.361	0.167
	t_2	0.751	1.000	0.789	0.456
	t_3	0.361	0.789	1.000	0.765
	t_4	0.167	0.456	0.765	1.000
10^{-12}	t_1	1.000	0.710	0.345	0.150
	t_2	0.710	1.000	0.757	0.383
	t_3	0.345	0.757	1.000	0.720
	t_4	0.150	0.383	0.720	1.000

It is clear from Tables 2 and 3 that the correlation coefficients between LLF for different time are essentially smaller than those for different wavelengths. Therefore, taking into account the LLF fluctuations with time when solving the inverse problem to determine the instantaneous gas concentrations gives no effect.

Statistical description of the molecular absorption characteristics

Among molecular gases for which the operation of the remote gas analyzer was simulated, two components − H$_2$O and CO$_2$ − are interfering gases. They are always present along the sounding path, and their absorption coefficients can vary randomly in time and space because of random fluctuations of temperature and their partial pressure. To provide for complete statistical description of the coefficients of NH$_3$-laser radiation absorption by these gases, many-year series of observations over meteorological parameters for the region of measurements are needed. The data on the mean values of temperature and pressure, as well as the variances of these parameters are included in zonally mean climatic models, such as, for example, the AFGL model[9] or the model of the Institute of Atmospheric Optics (IAO).[10] However, within the framework of a model for a given region, significant deviations from the situation described by the model are possible.

The comparison of the mean temperature and humidity values by the IAO model with the data of the 10-year observation series (1961 − 1970) at the Novosibirsk weather station shows that the mean values of these parameters are close for the summer conditions, whereas the corresponding mean values for winter are closer to the data of the AFGL sub-arctic model.

The rms temperature deviations are well described by the IAO model, but the rms humidity deviations by this model are twice as large as those by the data of the Novosibirsk weather station (Table 4). This situation is caused by a global character of the zonally mean models in any version. When designing and using open-path gas analyzers, it is preferable to use regional models, since they are more adequate to meteorological situations at the territory where the gas analyzer operates.

Table 4. Comparison of the zonally mean meteorological models with the data of observation at the Novosibirsk weather station

Model	T, K	rms	P_{H_2O}, mbar	rms
Mid-latitude summer, IAO model	292.0	7.3	15.6	6.1
Summer, Novosibirsk	290.9	6.1	14.4	3.6
Winter, AFGL sub-arctic model	257.2	−	1.41	−
Winter, Novosibirsk	255.0	10.2	1.51	1.2

Statistical characteristics of the optical depth due to water vapor and carbon dioxide molecular absorption were calculated for the summer and winter conditions by the data of the Novosibirsk weather station. For every realization of temperature and humidity, the optical depth was calculated by the direct method for all the 35 wavelengths at which NH_3 laser emits. We ignored variations in the CO_2 concentration, because changes of the CO_2 absorption coefficient due to temperature variations are far larger than those due to variations in the concentration.[11,12] Besides, summer conditions for which the absorption by carbon dioxide is far smaller than the absorption by water vapor are of the greatest interest.

Table 5. Summer. Descriptive statistics of the optical depth due to H_2O and CO_2 absorption along the horizontal path 4 km long

No.	λ, μm	ν, cm^{-1}	Mean	Min	Max	rms
1	13.1498	760.468	3.162	1.430	5.24	0.809
2	13.1459	760.693	2.674	0.980	4.88	0.836
3	13.1248	761.916	2.393	1.180	3.86	0.560
4	13.1123	762.643	1.293	0.330	2.63	0.484
5	13.0311	767.395	1.601	0.480	3.10	0.566
6	12.9716	770.915	1.388	0.408	2.73	0.492
7	12.9195	774.024	1.388	0.440	2.69	0.479
8	12.8789	776.464	2.011	0.656	3.77	0.671
9	12.8487	778.289	1.397	0.377	2.77	0.508
10	12.8112	780.567	1.293	0.374	2.55	0.461
11	12.6891	788.078	1.146	0.267	2.35	0.439
12	12.6306	791.728	2.318	1.280	3.55	0.477
13	12.5906	794.243	2.013	0.668	3.78	0.672
14	12.5607	796.134	6.364	2.480	10.90	1.818
15	12.5400	797.448	4.051	1.360	7.36	1.287
16	12.5278	798.225	4.125	1.620	7.16	1.192
17	12.3500	809.717	1.027	0.240	2.10	0.393
18	12.3107	812.301	0.967	0.234	1.98	0.367
19	12.2814	814.239	1.841	0.604	3.46	0.615
20	12.2610	815.594	1.124	0.358	2.17	0.386
21	12.2491	816.387	1.013	0.244	2.06	0.385
22	12.2451	816.653	0.948	0.214	1.96	0.367
23	12.0797	827.835	3.320	1.150	5.96	1.038
24	12.0791	827.876	2.339	0.820	4.24	0.740
25	12.0101	832.633	0.823	0.180	1.71	0.322
26	11.9902	834.014	0.823	0.179	1.71	0.322
27	11.7271	852.726	4.845	1.500	9.48	1.635
28	11.7158	853.548	1.147	0.349	2.20	0.400
29	11.5271	867.521	0.707	0.155	1.47	0.276
30	11.5245	867.717	0.707	0.155	1.47	0.276
31	11.4714	871.733	0.794	0.205	1.58	0.291
32	11.4604	872.570	0.682	0.153	1.41	0.264
33	11.0119	908.109	0.690	0.179	1.38	0.255
34	11.0111	908.174	0.669	0.170	1.34	0.248
35	11.0108	908.199	0.670	0.170	1.34	0.248

The results of statistical analysis given in Table 5 allow some conclusions to be drawn. Absorption of the NH_3-laser radiation by water vapor and carbon dioxide along the horizontal path can vary quite widely. So, for example, the mean value of the optical depth for the summer conditions can vary from 0.67 to 6.38 with the maximum spread from 0.17 to 10.90. The mean optical depth for the winter conditions varies from 0.30 to 0.635 with the maximum spread from 0.001 to 2.16.

For the winter conditions the optical depth distribution function is well described by the gamma distribution, while for the summer conditions it is well described by the distribution function of the normal type.

Analysis of errors in reconstruction of gas concentrations from the data of an NH_3-laser-based remote spectrometer

The problem to determine the total gas content along the horizontal path in the multiwave laser sounding is usually reduced to the linear regression analysis in which the gas concentration is determined from solution of the set of linear equations

$$y_i = y_0 + \sum_{j=1}^{n} k_{ij}\, x_j + \delta_i, \qquad (26)$$

where $y_i = \ln(I_i / I_{0i})$ is the logarithm of the intensity ratio of the radiation having passed through a medium to the incident radiation at the wavelength λ_i; k_{ij} is the coefficient of absorption of the jth gas at the ith wavelength; x_j is the sought gas concentration; y_0 is the constant.

The classical regression analysis is based on the assumption that the error δ_i is a random parameter distributed by the normal law. Its values are not correlated and have the same variances at different wavelengths. The matrix of the absorption coefficients is not random. This means that its elements are the known values exactly set by an investigator, and, moreover, a rank of this matrix equals the number of the unknowns.

The analysis has shown that for the lidar under study the above-mentioned conditions can break down due to the following factors.

1. Spontaneous spectral trends caused by aerosol extinction and turbulent losses, as well as errors in initial spectroscopic data can result in the wavelength dependence of the error and correlation between them. Deviation of the distribution function of the loss factor from the normal type can cause additional inhomogeneity in the data.

2. Wide variability of atmospheric meteorological conditions along the path, on the one hand, and the limited dynamic range of the receiving system, on the other hand, can cause the laser radiation received at some wavelengths to become comparable with the level of the receiver noise because of large energy losses. At the same time, for other wavelengths at which the selective absorption is small, the measured signal can fall outside the linear part of the voltage characteristic of the recording system. These factors can lead to errors in solution of the inverse problem.

To actually describe the process of sounding and solution of the inverse problem, laser radiation extinction caused by air molecules (H_2O, CO_2, NH_3, HCN, and HNO_3), aerosol, turbulent distortions of the beam, and its incomplete interception was taken into

account. Spectroscopic errors, photodetector noise, and background radiation of the atmosphere were taken into account too.

The laser radiation spectrum was modeled using the data from Ref. 3 and the HITRAN−96 database[13] with the refined laser wavelengths. The model spectrum is shown in Fig. 9.
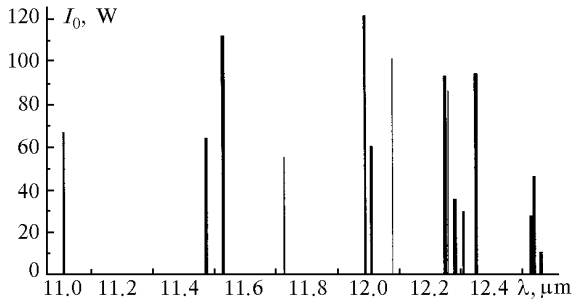
Fig. 9. Model spectrum of the NH$_3$-laser radiation.

To describe the aerosol extinction, we used the data from Refs. 14 and 15 which are generalizations of long series of actual observations over the ground aerosol. These papers present the mean values and rms deviations of the aerosol extinction coefficients in the 8 − 12 μm spectral range for the urban haze (summer and winter conditions). The optical depth τ_i^a due to aerosol extinction was assumed a random value generated by the random-number generator and distributed by the lognormal law; the mean values and rms deviations were set corresponding to the model of the urban haze.[14,15]

One of the factors attenuating the NH$_3$-laser radiation in the 8−12 μm window is the H$_2$O continuum absorption. In spite of the huge number of publications dedicated to this problem, it should be stated that uncertainties in the quantitative data are quite considerable,[16−19] especially for low concentrations of water vapor. In this connection, such techniques are preferable to be used for solution of the inverse problem, which allow the continuum absorption to be excluded along with the aerosol extinction.

The aerosol extinction, H$_2$O continuum absorption, and turbulent distortions of the laser beam have the spectral dependence which can change from the neutral to monotonically increasing one with the wavelength depending on the propagation conditions along the path (Fig. 10). It should be noted that for low water vapor concentrations the situations are also possible when the optical depth τ decreases with the wavelength. It is impossible to predict the behavior of this spectral dependence. So, when solving the inverse problem, it is necessary to provide for exclusion of these trends.

The spectroscopic error Δ_i^s was calculated as

$$\Delta_i^s = \sum_{j=1}^{n} \delta_{ij} \, k_{ij} \, x_j, \qquad (27)$$

where δ_{ij} is the normally distributed random parameter generated by the random-number generator.
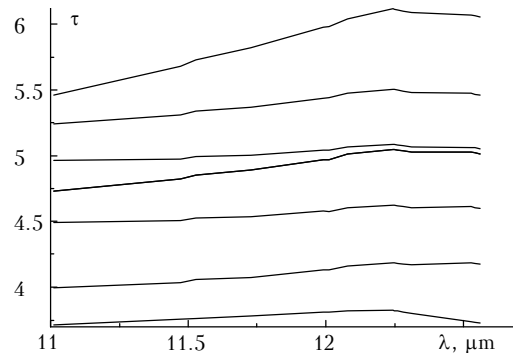
Fig. 10. Spectral behavior of τ caused by the combined effect of the H$_2$O continuum absorption, aerosol extinction (urban haze), turbulent losses ($C_n^2 = 10^{-13}$ m$^{-2/3}$), incomplete interception of the beam, and losses of the receiving system under summer conditions.

The errors in calculation of the CO$_2$ molecular absorption coefficients are caused by inaccuracy of the *a priori* spectroscopic information estimated based on the HITRAN database by the technique described in Ref. 20 as varying within 5 − 8%.

To analyze the errors in the H$_2$O and NH$_3$ absorption coefficients, the calculated data were compared with the data of laboratory measurements in the 8−12 μm spectral range with the use of the CO$_2$ laser. The largest differences of the calculated H$_2$O absorption coefficients from the experimental ones[16−19] were observed at those wavelengths where selective absorption is small. Therefore, a conclusion on the poor quality of the spectroscopic information for weak lines can be drawn. The NH$_3$-laser radiation spectrum falls in the region containing strong H$_2$O absorption lines. So, the value about 10% was taken as an estimate of the relative rms error in calculation of the H$_2$O selective absorption coefficients. The comparison of the experimentally measured NH$_3$ absorption coefficients[21−24] with the calculated ones led us to the conclusions similar to those drawn in the analysis of the H$_2$O data. For the ammonia absorption coefficients exceeding 1 atm^{-1}·cm^{-1} the relative rms error is approximately 10%.

The thermal noise of photodetector was generated by the random-number generator at the threshold value of 1 mW. Readouts at the wavelengths for which the signal value did not fall within the dynamic range of the receiving system (signal − noise = 10^4) were rejected during the simulation. It was assumed that the minimum signal value which still can be recorded must twice exceed the noise level.

The inverse problem was solved by the method of least squares for two schemes: without correction of the spectral trend (model described by Eq. (26)) and with correction

$$y_i = y_0 + \beta \, (\lambda_i - \lambda_0) / \Delta\lambda + \sum_{j=1}^{n} k_{ij} \, x_j + \delta_i. \qquad (28)$$

Ignoring the trend gives shifted solutions. The correction for it eliminates this shift, but leads, as a rule, to a worse plan matrix and higher condition number. The spectroscopic errors also give the shifted solution,[25,26] and the increase in the condition number leads to the increase in this shift. In this connection, it was interesting to find the conditions under which the solution is improved by allowing for the trend.

Seven parameters were taken into account: gas concentrations, as well as y_0 and β entering into Eq. (28). The last two parameters describe the summary losses along the path caused by incomplete interception of the beam, turbulence, and continuum absorption. Because the simulation was performed for a wide variability range of atmospheric conditions along the path, these seven factors were not always significant. So, for example, the water vapor concentration is small under winter conditions, and in some cases it can be ignored while solving the inverse problem.

For every situation a series of size 200 was simulated taking into account and ignoring the spectroscopic errors, and the mean values of the residual variance D were calculated, as well as the reconstructed concentrations and their rms deviations calculated from the obtained sample. These parameters allowed integral estimation of the influence of the spectroscopic errors and the combined effect of turbulent distortions, H_2O continuum absorption, and aerosol extinction on the accuracy of solution of the inverse problem.

Table 6. Winter, minimal content of H_2O

C_n^2	Trend**	Δ_s	N_g	C_0, atm	C, atm	σ_C, atm
14	1	1	1*	−9.52E−05	−4.62E−04	1.0E−03
			2*	3.30E−04	6.69E−04	5.3E−03
	$D = 3.12$E−2		3	5.00E−07	5.13E−07	7.0E−08
			4*	5.00E−08	6.25E−08	6.9E−08
			5*	1.70E−07	−9.55E−06	8.9E−05
14	1	0	1*	9.52E−05	−1.20E−04	1.4E−04
			2*	3.30E−04	7.84E−04	3.3E−04
	$D = 3.8$E−04		3	5.00E−07	5.17E−07	8.8E−09
			4	5.00E−08	7.09E−08	1.2E−08
			5*	1.70E−07	3.32E−06	8.2E−06
14	1	1				
	$D = 2.9$E−2		3	5.00E−07	5.02E−07	6.4E−08
14	0	1				
	$D = 3.2$E−2		3	5.00E−07	5.05E−07	5.2E−08
14	1	0				
	$D = 3.5$E−3		3	5.00E−07	5.01E−07	7.1E−9
14	0	0				
	$D = 4.4$E−3		3	5.00E−07	5.09E−07	3.3E−09
12	1	1	1*	9.52E−05	1.05E−04	9.1E−05
			2*	3.30E−04	1.67E−03	4.2E−03
	$D = 3.1$E−2		3	5.00E−07	5.29E−07	7.1E−08
			4*	5.00E−08	5.84E−08	7.6E−08
			5*	1.70E−07	4.42E−06	19. E−06
12	1	0	1*	9.52E−05	−1.37E−04	1.7E−04
			2*	3.30E−04	8.05E−04	3.2E−04
			3	5.00E−07	5.19E−07	1.2E−08
	$D = 2.7$E−04		4	5.00E−08	7.23E−08	1.5E−08
			5*	1.70E−07	−3.02E−06	6.6E−06
12	1	1				
	$D = 2.7$E−2		3	5.00E−07	5.01E−07	5.0E−08
12	0	1				
	$D = 2.9$E−2		3	5.00E−07	5.12E−07	5.4E−08
12	1	0				
	$D = 3.8$E−3		3	5.00E−07	5.01E−07	6.8E−10
12	0	0				
	$D = 4.4$E−3		3	5.00E−07	5.09E−07	3.1E−09

* We failed to reconstruct concentrations of these gases. N_g is the number of the gas: H_2O (1), CO_2 (2), NH_3 (3), HNO_3 (4), and HCN (5).

** The digit "0B means that the trend was neglected, and "1B means that the trend was taken into account. Δ_s is the spectroscopic error, "0B means that it was neglected, and "1B means that it was taken into account. C_0 are the initial gas concentrations; C are the reconstructed concentrations; σ_C is the rms deviation of C; D is the mean value of the residual variance for a sample.

Table 7. Summer, medium content of H$_2$O

C_n^2	Trend**	Δ_s	N_g	C_0, atm	C, atm	σ_C, atm
14	1	1	1	1.31E−02	1.31E−02	0.09E−02
			2*	3.30E−04	3.63E−04	3.4E−04
			3	5.00E−07	4.75E−07	0.8E−08
D = 6.8E−2			4*	5.00E−08	−1.03E−08	15.E−08
			5*	1.70E−07	4.42E−06	19.E−06
14	1	0	1	1.31E−02	1.31E−02	3.9E−05
			2	3.30E−04	3.75E−04	2.2E−06
			3	5.00E−07	5.09E−07	2.9E−09
D = 2.7E−04			4	5.00E−08	6.07E−08	7.5E−09
			5*	1.70E−07	2.01E−06	6.2E−07
14	1	1	1	1.31E−02	1.30E−02	7.9E−04
D = 6.5E−2			3	5.00E−07	4.71E−07	5.1E−08
14	0	1	1	1.31E−02	1.30E−02	8.2E−04
D = 5.8E−2			3	5.00E−07	4.77E−07	5.3E−08
14	1	0	1	1.31E−02	1.31E−02	3.4E−05
D = 2.9E−3			2	5.00E−07	4.88E−07	8.3E−10
14	0	0	1	1.31E−02	1.31E−02	3.3E−05
D = 2.9E−3			2	5.00E−07	4.81E−07	1.3E−09
13	1	1	1	1.31E−02	1.32E−02	9.8E−04
			2*	3.30E−04	3.28E−04	3.4E−04
			3	5.00E−07	4.88E−07	8.2E−08
D = 6.2E−02			4*	5.00E−08	1.93E−08	16.1E−08
			5*	1.70E−07	4.83E−06	19.6E−06
13	1	0	1	1.31E−02	1.31E−02	3.4E−05
			2	3.30E−04	3.80E−04	3.0E−06
			3	5.00E−07	5.11E−07	2.4E−09
D = 2.7E−04			4	5.00E−08	6.38E−08	6.0E−09
			5*	1.70E−07	2.02E−06	4.8E−07
13	1	1	1	1.31E−02	1.30E−02	8.1E−04
D = 6.2E−02			3	5.00E−07	4.67E−07	4.6E−08
13	0	1	1	1.31E−02	1.30E−02	8.6E−04
D = 6.7E−2			3	5.00E−07	4.67E−07	5.2E−08
13	1	0	1	1.31E−02	1.31E−02	2.9E−05
D = 3.1E−3			3	5.00E−07	4.89E−07	7.1E−10
13	0	0	1	1.31E−02	1.31E−02	3.0E−05
D = 4.0E−3			3	5.00E−07	4.75E−07	7.4E−09
12	1	1	1	1.31E−02	1.33E−02	4.9E−03
			2*	3.30E−04	3.21E−04	3.5E−04
			3	5.00E−07	4.89E−07	8.1E−08
D = 3.8E−2			4*	5.00E−08	2.32E−08	13.2E−08
			5*	1.70E−07	6.30E−06	58.6E−06
12	1	0	1	1.31E−02	1.30E−02	4.9E−03
			2	3.30E−04	3.57E−04	5.7E−05
			3	5.00E−07	5.03E−07	3.7E−08
D = 3.9E−4			4	5.00E−08	6.13E−08	3.1E−08
			5*	1.70E−07	−7.21E−06	67.1E−06
12	1	1	1	1.31E−02	1.33E−02	2.0E−03
D = 3.8E−2			3	5.00E−07	4.67E−07	5.2E−08
12	1	0	1	1.31E−02	1.34E−02	1.9E−04
D = 3.6E−3			3	5.00E−07	4.82E−07	1.3E−08
12	0	1	1	1.31E−02	1.32E−02	4.4E−03
D = 4.7E−2			3	5.00E−07	4.54E−07	5.4E−08
12	0	0	1	1.31E−02	1.35E−02	2.1E−03
D = 9.7E−3			3	5	4.74E−07	2.2E−08

N o t e . Explanations for Table 7 the same as for Table 6.

Tables 6 and 7 give the results of numerical simulation of reconstruction of the gas concentrations. It is clear from these tables that the spectroscopic errors exert the strongest effect on solution of the inverse problem. Taking into account the spectroscopic errors leads to the increase of the residual variance D. For the gas composition considered it proved possible to reconstruct the concentration of only one gas, NH$_3$,

under winter conditions and two gases, NH_3 and H_2O, under summer conditions. In the case of absence of the spectroscopic errors the concentrations can be reconstructed for two gases, NH_3 and HNO_3, under winter conditions and for four gases, H_2O, CO_2, NH_3, and HNO_3, under summer conditions. The concentration of only one gas was determined under winter conditions mainly because of the low temperature which leads to low humidity and to the decrease in the HNO_3 and CO_2 absorption coefficients.

Taking into account or ignoring the trend in solution of the inverse problem did not markedly change the value of the residual variance. The effect of the trend showed itself mainly in the value of the rms deviation of the reconstructed concentrations. Taking into account the trend allowed this deviation to be decreased. Comparing Tables 6 and 7 allows we can draw the conclusion that the governing role in formation of the trend belongs to the H_2O continuum absorption.

It should be noted that at high humidity and large aerosol extinction coefficients the strong turbulence can lead to marked errors in solution the inverse problem. However, this is mainly caused by high losses along the path, rather than turbulent distortions of the beam. An example of solution of the inverse problem under these conditions is shown in Fig. 11. For the samples No. 39 and 65 the losses along the path were such that the number of equations decreased down to five and four, respectively, for the four unknowns. Just this has led to the maximum errors in this series.
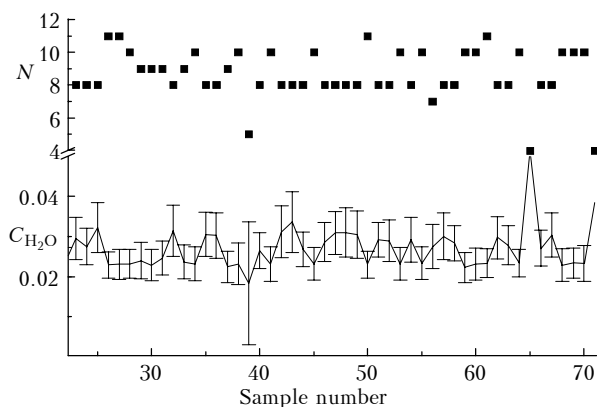

Fig. 11. An example of reconstruction of the m_2n concentration for the summer conditions ($C_{H_2O} = 0.0232$ atm, $C_n^2 = 10^{-12}$ m$^{-2/3}$). The vertical bars correspond to the 95-% confidence intervals. The squares show the number of equations (the number of wavelengths at which the intensity of the passed radiation exceeds the noise).

Conclusion

Extinction of the NH_3-laser radiation in the actual atmosphere along the horizontal path 4 km long can vary quite widely. For the summer conditions the maximum spread of the optical depth due to H_2O and CO_2 absorption is 0.17 to 10.90, and for the logarithmic loss factor for $C_n^2 = 10^{-12}$ m$^{-2/3}$ it is 3.3 to 10.8. For reliable recording of signals the receiver must have the sufficiently wide dynamic range.

The results obtained from solution of the inverse problem allow the conclusion that taking into account the spectral trend compensates for turbulent distortions of the beam. The main source of errors is inaccuracy of the spectroscopic information which can lead to a marked shift of the solution with respect to the actual values of the gas concentrations. There are two ways to increase the accuracy of gas analysis. The first and most reliable way is to conduct high-accuracy measurements of the molecular absorption coefficients. Another way is to conduct measurements with an open-path spectrometer based on the NH_3 laser with a set of calibrating cells containing the gases to be measured with the known concentrations and then to use statistical methods allowing the inhomogeneity due to spectroscopic errors to be revealed in the observations.

References

1. M.W. Sigrist, ed., *Air Monitoring by Spectroscopic TechniCues* (Willey, New York, 1993), 530 pp.
2. A. Olafsson and M. Phammerich, *Trace Gas Detection with IR Gas Lasers*, ed. by W. Demtroder (1990) 403 pp.
3. V.Yu. Baranov, I.V. Bobkov, A.P. Dyad'kin, D.D. Malyuta, V.S. Mezhevov, V.A. Kuz'menko, G.A. Polyakov, S.V. Pigul'skii, A.N. Starostin, and A.A. Khakhalev, "*Multiwave Ammonia Lidar,*B Preprint No. 0043-A, Troitsk Institute of Innovation and Thermonuclear Investigation, Moscow (1998), 49 pp.
4. M. Born and E. Wolf, *Principles of Optics* (Pergamon press, New York, 1965).
5. V.P. Kandidov, Usp. Fiz. Nauk **166**, No. 12, 1309−1338 (1996).
6. V.I. Tatarskii, *Wave Propagation in a Turbulent Medium* (McGraw-Hill, New York, 1961).
7. A.S. Gurvich, A.I. Kon, V.L. Mironov, and S.S. Khmelevtsov, *Laser Radiation in the Turbulent Atmosphere* (Nauka, Moscow, 1976), 227 pp.
8. V.E. Zuev, V.A. Banakh, and V.V. Pokasov, *Optics of the Turbulent Atmosphere* (Gidrometeoizdat, Leningrad, 1988), 270 pp.
9. G.P. Anderson, S.A. Clough, F.X. Kneizys, J.H. Chetwynd, and E.P. Shettle, *AFGL Atmospheric Constituent Profiles (0-120 km)*, AFGL−TR−86−0110.AD A175173 (1986).
10. V.E. Zuev and V.S. Komarov, *Statistical Models of Temperature and Gaseous Constituents of the Atmosphere* (Gidrometeoizdat, Leningrad, 1986), 264 pp.
11. Yu.S. Makushkin, A.A. Mitsel', and K.M. Firsov, Izv. Akad. Nauk SSSR, Fiz. Atmos. Okeana **22**, No. 6, 595−599 (1986).
12. A.A. Mitsel' and K.M. Firsov, Atm. Opt. **3**, No. 5, 451−454 (1990).
13. L.S. Rothman, R. Gamache, R. Tipping, C. Rinsland, M. Smith, D. Benner, Devi V. Malathy, J.M. Flaud, C. Camy-Peyret, A. Perrin, A. Goldman, S. Massie, L. Brown, and R. Toth, J. Quant. Spectrosc. Radiat. Transfer **48**, 469−507 (1992).
14. Yu.A. Pkhalagov, V.N. Uzhegov, and N.N. Shchelkanov, Atmos. Oceanic Opt. **9**, No. 6, 455−458 (1996).

15. V.N. Uzhegov, Yu.A. Pkhalagov, and N.N. Shchelkanov, Atmos. Oceanic Opt. **7**, No. 8, 570–574 (1994).

16. N.N. Shchelkanov, Yu.A. Pkhalagov, and V.N. Uzhegov, Atmos. Oceanic Opt. **7**, 431–434 (1992).

17. V.N. Aref'ev, V.N. Pogodaev, and R.I. Sizov, Kvant. Elektron. **10**, No. 13, 496–502 (1983).

18. R.E. Roberts, J.E.A. Selby, and L.M. Biberman, Appl. Opt. **15**, No. 9, 2085 (1976).

19. S.A. Clough, F.X. Kneizys, and R.W. Davis, Atmos. Res. **23**, 229–241 (1989).

20. K.M. Firsov, A.A. Mitsel', O.V. Naumenko, and T.Yu. Chesnokova, Atmos. Oceanic Opt. **11**, No. 10, 923–933 (1998).

21. M.S. Shumate, R.T. Menzies, J.S. Margolis, and L.-G. Rozengren, Appl. Opt. **15**, No. 10, 2480–2488 (1976).

22. V.N. Aref'ev and K. Visheratin, Tr. Inst. Exp. Meteorol., Issue 12, 121–124 (1982).

23. R.R. Patty, G.M. Ruswirm, and W.A. McClenny, Appl. Opt. **13**, No. 12, 2850–2854 (1974).

24. R.J. Brewer and C.W. Bruce, Appl. Opt. **17**, No. 23, 3746–3749 (1978).

25. A. Afifi and S. Eizen, *Statistical Analysis. Computer Approach* (Mir, Moscow, 1982), 488 pp.

26. I. Vuchkov, L. Boyadzhieva, and E. Solakov, *Applied Linear Regression Analysis* (Finansy i Statistika, Moscow, 1987), 240 pp.